

Quasiparticle GW band structures and Fermi surfaces of bulk and monolayer NbS_2

Christoph Heil,^{1,2} Martin Schlipf,¹ and Feliciano Giustino^{1,3,*}

¹*Department of Materials, University of Oxford, Parks Road, Oxford OX1 3PH, United Kingdom*

²*Institute of Theoretical and Computational Physics, Graz University of Technology, NAWI Graz, 8010 Graz, Austria*

³*Department of Materials Science and Engineering,
Cornell University, Ithaca, New York 14853, USA*

(Dated: October 2, 2018)

In this work we employ the GW approximation in the framework of the Sternheimer GW method to investigate the effects of many-body corrections to the band structures and Fermi surfaces of bulk and monolayer NbS_2 . For the bulk system, we find that the inclusion of these many-body effects leads to important changes in the band structure, especially in the low-energy regime around the Fermi level, and that our calculations are in good agreement with recent ARPES measurements. In the case of a free-standing monolayer NbS_2 , we observe a strong increase of the screened Coulomb interaction and the quasiparticle corrections as compared to bulk. In this case we also perform calculations to include the effect of screening by a substrate. We report in detail the results of our convergence tests and computational parameters, to serve as a solid basis for future studies.

I. INTRODUCTION

Transition metal dichalcogenides (TMDs) have been the focus of many studies in recent years, as their physical and chemical diversity offers an ideal platform to investigate semiconductors, metals, and superconductors in layered systems using the same structural template [1–4]. Within the family of TMDs, metallic materials have attracted considerable attention due to the fact that both a superconducting phase as well as a charge density wave (CDW) phase appear in the low-temperature phase diagram [5–13]. Moreover, the fact that the increased spatial confinement in few-layer and monolayer systems, as well as the substrates they are placed on, cause important changes in the electronic structure [14], in particular in the screened Coulomb interaction, has drawn considerable interest to two-dimensional (2D) materials [15–22]. With respect to few-layer TMDs, experiments show that the superconducting critical temperature tends to decrease with decreasing number of layers [21, 23, 24]. The situation for the critical temperature of the CDW order is less clear, and a consensus on how it depends on the layer thickness has not yet been achieved [21, 24–26].

The metallic compound $2H\text{-NbS}_2$ stands out in the TMD family, as it is superconducting with a critical temperature of ~ 6 K, but does not exhibit CDW order in the bulk. It has recently been proposed that bulk NbS_2 is actually on the verge of a CDW instability [27]. The strongly anharmonic phonon modes dominate the superconducting pairing in $2H\text{-NbS}_2$, successfully explaining the two-gap feature observed in experiments. In Ref. 27 it is shown that accurate low-energy band structures and Fermi surfaces beyond density-functional theory (DFT) are crucial for achieving a better quantitative agreement with experiments. At variance with bulk NbS_2 , the fabrication and experimental investigation of monolayer NbS_2 has not been reported yet.

In the present study, we want to expand on these findings and provide an extensive view on the electronic properties of bulk and monolayer NbS_2 beyond DFT by con-

sidering many-body perturbation theory in the framework of the GW approximation [28–33]. In addition, as only few GW calculations have been reported for metallic TMDs [34], part of this work is to examine the various convergence parameters of the GW calculation for the bulk and the monolayer system. As the main focus of this work, we compare our calculations with recent angle-resolved photoemission spectroscopy (ARPES) measurements on bulk NbS_2 [35]. Furthermore, we assess the effects of the increased spatial confinement when going from bulk to the monolayer, and the role of substrates. We discuss comparisons of the DFT-derived electronic structures with the quasiparticle (QP) band structures to shed light on the effects of many-body interactions.

This paper is organized as follows: In Sec. II, we provide structural details about bulk and monolayer NbS_2 , we give a short overview of the methods used in this work, and summarize the computational setup and the convergence properties of the GW calculations. In Sec. III we discuss our results for the band structures, densities of states, and Fermi surfaces of bulk and monolayer NbS_2 . In the case of bulk NbS_2 we compare our calculations with recent ARPES data. In Sec. IV, we offer our conclusions and identify important avenues of future research. In the appendixes we report detailed convergence tests of the GW calculations with respect to plane waves, energy cutoffs, and Brillouin-zone sampling.

II. COMPUTATIONAL DETAILS

A. Structures

Bulk $2H\text{-NbS}_2$ crystallizes in a layered hexagonal structure with space group $P6_3/mmc$. The unit cell contains two S-Nb-S layers, as shown in Fig. 1. The Nb atoms occupy the $2b$ Wyckoff positions $(0, 0, 1/4)$ and the S atoms are located at the $4f$ positions $(1/3, 2/3, z)$. All calculations are performed in the optimized crystal structure, with lattice parameters $a = 3.28 \text{ \AA}$, $c/a = 3.47$,

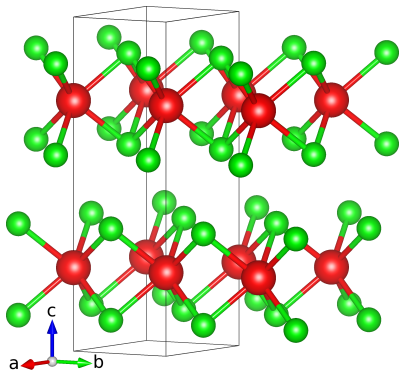


Figure 1. Ball-and-stick model of the unit cell of $2H\text{-NbS}_2$. Nb atoms are shown in red, and S atoms in green.

and $z = 0.113$.

The NbS_2 monolayer is simulated by replacing one of the two S-Nb-S layers in the unit cell by a vacuum region of 10 \AA . In order to avoid artificial effects from the nonperiodic z direction in the 2D calculations, the bare Coulomb interaction is truncated along the non-periodic dimension for both the correlation and the exchange part of the self-energy [36]. We checked that the changes in our results due to an increase of the vacuum region are negligible. In the monolayer, the inversion symmetry is broken, so that spin-orbit coupling (SOC) will induce a Rashba-Dresselhaus splitting [37, 38] of the bands. However, the authors of Ref. 39 showed that the effects of including SOC in GW calculations for a related chalcogenide are small. Hence, it should be sufficient to evaluate the magnitude of the spin splitting on the level of DFT and impose the same splitting on the GW results. Kim and Son [34], for example, investigated the SOC effects along these lines in the isoelectric and isostructural NbSe_2 . As we show in Appendix A, for both bulk (Fig. 11) and monolayer NbS_2 (Fig. 12) the effects of including SOC on the level of DFT is smaller than the changes in the electronic structure due to GW corrections, allowing us to neglect SOC in a first approximation and solely focus on the changes of the electronic structure arising from the inclusion of many-body perturbation theory. We also tested the influence of including van der Waals (vdW) corrections at the step of the structure optimization within DFT on our GW results, and found the changes to be very small. Hence, in order to avoid any confusion, all the results in the main part of the paper are performed without vdW corrections, and a discussion on the effects of including vdW forces is provided in Appendix B.

B. Methodology

First-principles DFT calculations [40] generally yield accurate predictions for ground-state properties such as structural parameters or the response to static electric

and magnetic fields. The predictive power is less impressive when it comes to electronic excitations. For example, Kohn-Sham DFT tends to yield too low band gaps, as well as inaccurate band widths, densities of states, and effective masses [41]. Among the possible approaches to overcome these limitations, such as for example hybrid functionals, the quasiparticle GW method has emerged as one of the most reliable tools across the materials spectrum, such as semiconductors, insulators, and metals, bulk systems, as well as surfaces and interfaces [28–31]. In this method, the exchange-correlation potential V_{xc} is replaced by the system’s self-energy Σ , and the QP energies are obtained by performing a perturbative expansion of Σ and the dielectric function ϵ . By doing so, this method is free of the previously mentioned self-interactions and also reproduces the nonanalytic behavior when the particle number changes.[42] This permits us to study a wide range of diverse materials, from solids to molecules and nanostructures, as well as surfaces and interfaces [43, 44]. Important applications include the correction of band gaps and bandwidths [45], and while GW has traditionally been used for insulators and semiconductors, it is expected to affect the properties of metallic systems as well.

All these advantages, however, require a considerably heavier computational workload compared to DFT methods. Specifically, traditional GW approaches show a very slow convergence with respect to unoccupied Kohn-Sham states [46]. To deal with these issues, Refs. 32 and 33 developed a method to calculate the self-energy without the need to consider unoccupied states. In this approach, both the Green’s function and the screened Coulomb interaction are determined by evaluating the Sternheimer equations in linear response [47–49], as originally proposed in Ref. 50 and also demonstrated in Refs. 51 and 52. To this end, the Green’s function $G(\mathbf{r}, \mathbf{r}'; \omega)$ and the screened Coulomb interaction $W(\mathbf{r}, \mathbf{r}'; \omega)$ are written as functions of \mathbf{r}' , and the space variable \mathbf{r} and the frequency ω are considered as parameters.[53] The Green’s function is given by

$$\left(\hat{H} - \omega\right) G_{[\mathbf{r}, \omega]} = -\delta_{\mathbf{r}}, \quad (1)$$

where \hat{H} represents the effective single-particle Hamiltonian. To obtain the first-order variations to the occupied electron states $\Delta\psi_{\nu[\mathbf{r}, \omega]}^{\pm}$ corresponding to the perturbation $\Delta V_{[\mathbf{r}, \omega]}(\mathbf{r}')$, one has to evaluate the two Sternheimer equations:

$$\left(\hat{H} - \epsilon_{\nu} \pm \omega\right) \Delta\psi_{\nu[\mathbf{r}, \omega]}^{\pm} = -\left[\theta(\epsilon_{\nu}) - \hat{P}_{\nu}\right] \Delta V_{[\mathbf{r}, \omega]} \psi_{\nu[\mathbf{r}, \omega]}^{\pm}. \quad (2)$$

Here, the operator \hat{P}_{ν} projects onto the subspace of occupied states, with the index ν running over only occupied electron states. $\theta(\epsilon_{\nu})$ accounts for the partial occupation in the case of a metallic system [54]. The first-order variation within the random-phase approximation (RPA) to

the single-particle density matrix $\Delta n_{[\mathbf{r},\omega]}$ reads

$$\Delta n_{[\mathbf{r},\omega]} = 2 \sum_{\nu} \psi_{\nu}^* \left(\Delta \psi_{\nu[\mathbf{r},\omega]}^+ + \Delta \psi_{\nu[\mathbf{r},\omega]}^- \right). \quad (3)$$

In Eq. (3), the prefactor 2 takes into account the spin degeneracy and the superscript + (−) refers to the positive (negative) frequency component of the induced charge. In the case of the perturbation being set to the bare Coulomb interaction, i.e., $\Delta V_{[\mathbf{r},\omega]}(\mathbf{r}') = v(\mathbf{r}, \mathbf{r}')$, the variation of the density matrix can be related to the dielectric matrix via [32]

$$\epsilon(\mathbf{r}, \mathbf{r}', \omega) = \delta(\mathbf{r}, \mathbf{r}') - \Delta n_{[\mathbf{r},\omega]}, \quad (4)$$

and the screened Coulomb interaction W can then be obtained by inverting this matrix,

$$W(\mathbf{r}, \mathbf{r}', \omega) = \int d\mathbf{r}'' v(\mathbf{r}, \mathbf{r}'') \epsilon^{-1}(\mathbf{r}'', \mathbf{r}', \omega). \quad (5)$$

Another possibility to solve the Sternheimer equations would be to set the perturbation $\Delta V_{[\mathbf{r},\omega]}(\mathbf{r}') = W(\mathbf{r}, \mathbf{r}', \omega)$, in which case the variation of the density yields a Hartree potential screening of the bare Coulomb interaction. The disadvantage of this approach is that Eq. (2) then needs to be solved self-consistently. For small systems, as for example the NbS₂ compounds considered in this work, the direct method outlined in Eqs. (4) and (5) is advantageous, due to the fact that the inversion of ϵ can be performed without a significant computational overhead. On the other hand, the self-consistent approach lends itself to being employed for larger systems and in cases where memory restrictions need to be met.

In short, the Sternheimer GW method has the advantages (i) to be able to disregard all unoccupied states from the calculation, which often cause convergence problems in conventional GW approaches [55], (ii) an improved accuracy with a similar or even smaller workflow compared to traditional GW methods, and (iii) the fact that a single parameter, i.e., the kinetic-energy cutoff of the inverse dielectric matrix, controls the QP energy convergence. The above procedure also provides the complete Green's function and screened Coulomb interaction, which enables the calculation of the complete self-energy.

In the following, we will report the results of GW calculations for bulk and monolayer NbS₂. These calculations have been performed at the G_0W_0 level with the SternheimerGW code [56]. We recalculated the Fermi level using the G_0W_0 quasiparticle eigenvalues to ensure the number of electrons is conserved [57]. We employed the RPA for the density response, and the frequency integration has been performed using the Godby-Needs plasmon-pole approximation [58], using an imaginary pole energy of 4 eV. The frequency integration was performed on the imaginary axis and the self-energy on the real axis was obtained with an analytic continuation using Padé approximants of order 11 [32, 33, 59]. We

employed scalar-relativistic optimized norm-conserving pseudopotentials [60] including the semi-core electrons of Nb. We used the LDA exchange-correlation functional [61] in the Perdew-Zunger (PZ) parametrization [62] and an electronic smearing of 5 mRy. Our convergence studies, which we report in detail in Appendixes C and D, show that the following parameters are sufficient to describe the electronic states with an accuracy of ~ 100 meV. For bulk NbS₂ we employed a kinetic-energy cutoff for the plane waves of the ground-state DFT calculation of 40 Ry (cf. Appendix C 1), a $12 \times 12 \times 4$ \mathbf{k} mesh (cf. Appendix C 2), an energy cutoff of 10 Ry for the dielectric matrix (cf. Appendix C 3), and an energy cutoff of 25 Ry for the exchange part of the self-energy (cf. Appendix C 4). For monolayer NbS₂ we employed a kinetic-energy cutoff for the plane waves of the ground-state DFT calculation of 40 Ry (cf. Appendix D 1), a $24 \times 24 \times 1$ \mathbf{k} mesh (cf. Appendix D 2), an energy cutoff of 10 Ry for the dielectric matrix (cf. Appendix D 3), and an energy cutoff of 25 Ry for the exchange part of the self-energy (cf. Appendix D 4).

We calculated the QP corrections to the Kohn-Sham eigenvalues for the bulk structure for a $6 \times 6 \times 2$ Brillouin-zone (BZ) grid and used maximally localized Wannier functions [63–65] to interpolate this data onto a fine $60 \times 60 \times 20$ BZ grid. For the monolayer, we interpolated from a coarse $8 \times 8 \times 1$ BZ grid to a fine $160 \times 160 \times 1$ BZ grid. In the case of the monolayer, the Coulomb interaction has been truncated in the z direction to account for the two-dimensional nature of the system.

III. RESULTS AND DISCUSSION

A. Bulk NbS₂

At first, we want to take a close look at the electronic band structures in the bulk compound. Compared to the LDA electronic structure, the inclusion of many-body interaction effects slightly increases the bandwidth of bulk 2H-NbS₂ for the electronic states up to ± 7 eV around the Fermi level [cf. Fig. 2(a)]. This increase originates mainly from the unoccupied bands being pushed to higher energies. We observe that at the Γ point, the S p_z and the Nb d_{z^2} states are pushed apart by the inclusion of electron-electron interactions. This is in contrast to the LDA case, where they are very close in energy. The single electron band crossing the Fermi level around the M point within LDA, which is of in-plane Nb $d_{xy}/d_{x^2-y^2}$ orbital character, is renormalized to lower energies. We will discuss the resulting change of the topology of the Fermi surface in more detail later in this paper. For the time being we only mention that the changes to the electronic structure, mostly around the M point, lead to a decrease of the DOS at the Fermi level by 18% [Fig. 2(d)]. As is pointed out in Ref. 27, this leads to a decreased electron-phonon coupling, and in turn to a lower critical superconducting temperature in this compound. At the

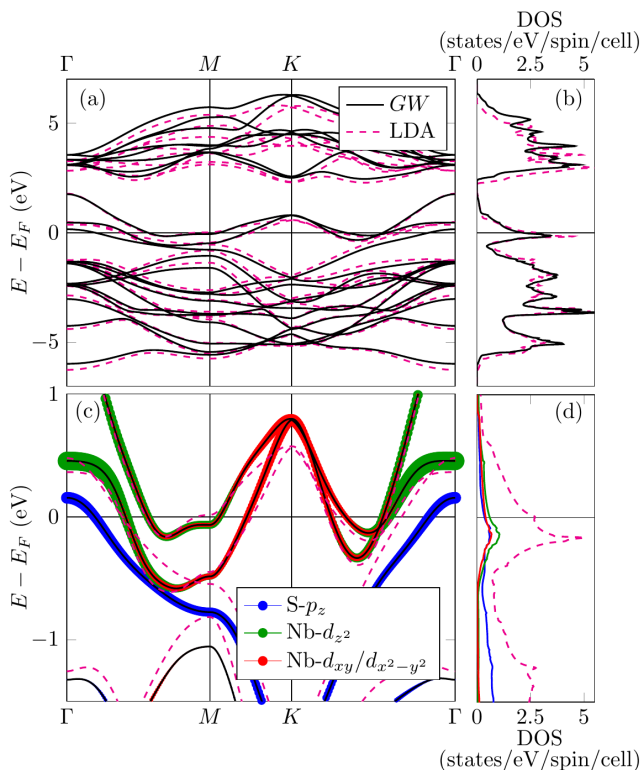


Figure 2. Comparison of the band structure (a), (c) and DOS (b), (d) of bulk $2H$ - NbS_2 on the level of LDA (dashed magenta) and with GW renormalization (solid black). In (c) and (d) we additionally provide the projection of the electronic states onto the $S p_z$ (blue), the out-of-plane $\text{Nb } d_{z^2}$ (green), and the in-plane $\text{Nb } d_{xy}/d_{x^2-y^2}$ (red) orbitals.

K point, we find that the unoccupied $\text{Nb } d_{xy}/x^2-y^2$ band is pushed to higher energies.

To better distinguish between the different effects the GW corrections have on the DFT electronic structure, we show the exchange-correlation potential V_{xc} , the exchange and correlation parts of the self-energy, Σ_x and Σ_c respectively, as well as the QP strength $Z_{n,\mathbf{k}} = (1 - \partial \text{Re} \Sigma_{n,\mathbf{k}} / \partial E)^{-1}$ and the QP correction (before the Wannier interpolation) as a function of the DFT eigenvalues in Fig. 3. The data points belonging to the Fermi-surface bands have been colored according to their largest orbital contribution, as detailed in Fig. 2. While V_{xc} is in very good approximation decreasing linearly with increasing DFT eigenvalue, Σ_x is increasing with an abrupt change around the DFT Fermi level, as depicted in Figs. 2(a) and 2(b) respectively. It is worth noting that Σ_x follows the standard trend of the exchange self-energy for the homogeneous electron gas, as is typical for metals exhibiting superconducting or magnetic phases at low temperatures [66]. The reverse trend to Σ_x is found for $\text{Re} \Sigma_c$, as shown in Fig. 3(c).

We find that in our calculations $Z_{n,\mathbf{k}}$ ranges from 0.54 to 0.71, showing that GW corrections decrease the QP strength considerably. In the case that the self-energy

is not explicitly \mathbf{k} dependent, which is in first approximation true for the Fermi-surface bands in NbS_2 , $Z_{n,\mathbf{k}}$ can be related to the velocity renormalization [67] via $1 - Z_{n,\mathbf{k}}^{-1} = (v_{n,\mathbf{k}} - v_{n,\mathbf{k}}^0) / v_{n,\mathbf{k}}$, with $v_{n,\mathbf{k}}$ and $v_{n,\mathbf{k}}^0$ being the interacting and noninteracting electron velocity, respectively. For bulk NbS_2 , we find a renormalization of the electron velocity at the Fermi level of around -51% . The Fermi velocity, as well as the mass renormalization around the Fermi level and the size of the Fermi surfaces, would be experimentally accessible by quantum oscillation measurements, like the de Haas van Alphen effect [68]. However, we are not aware of any such measurements for NbS_2 .

Plotting the QP corrections as function of the LDA eigenenergies, as depicted in Fig. 3(e), shows that the states above the Fermi level are experiencing a larger shift due to the inclusion of many-body perturbations compared to those below the Fermi level.

In Fig. 4, we compare the QP band structure with ARPES measurements from Ref. 35. We combined the reported experimental results obtained with horizontally and vertically polarized photons in Fig. 4(b). In order to account for the finite resolution in experiment, we broadened our band structure with Lorentzians with an energy-dependent full width at half maximum Γ , i.e., $\Gamma = \gamma |E - E_F| + \Gamma_0$ with $\gamma = 0.15$ and $\Gamma_0 = 0.15$ eV, to approximately match the experimental broadening. Our calculations agree with the ARPES measurements, reproducing all the major features observed in the experiments. In particular, the two excitations slightly above and below -2 eV at Γ and their further dispersion in the direction of the K point match the measurements nicely, as do the two partly occupied bands close to the Fermi level. The $S p_z$ band seems not to be visible in the ARPES data, probably due to a vanishing transition matrix element for the incident light beam. We further observe that a rigid shift of the Fermi level by 300 meV would bring the calculations in excellent agreement with the experiments, as shown in Fig. 4(c). This energy shift corresponds to adding 0.47 electrons per formula unit (f.u.) to the system, and could be explained by intrinsic doping effects or an imperfect stoichiometry of the sample. For example, the stoichiometry $\text{Nb}_{1.09}\text{S}_2$ would match the observed shift of 300 meV. Taking into account the accuracy of our GW calculations (~ 100 meV) and possible shifts in the band structure due to electron-phonon interaction (~ 50 meV) in the most favorable way, our calculations would also be in agreement with a stoichiometry of $\text{Nb}_{1.05}\text{S}_2$. These compositions for $\text{Nb}_{1+x}\text{S}_2$ are well within a range that has been realized in experiments [69]. Another possible source for the observed energy shift could be due to the fact that the G_0W_0 approach employed here is not a fully self-consistent method, hence the starting point of the calculation, i.e., the choice of the DFT functional, can be expected to slightly affect our results. Furthermore, as mentioned before, the G_0W_0 method does not conserve the particle number and the Fermi energy has

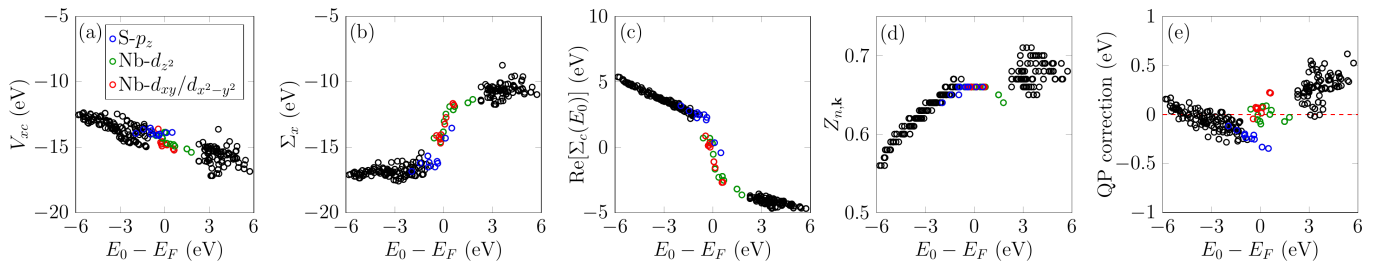


Figure 3. (a) Exchange-correlation potential V_{xc} , (b) exchange-part Σ_x of the self-energy, (c) real part of the correlation self-energy Σ_c at the DFT eigenvalues E_0 , (d) QP renormalization factor $Z_{n,\mathbf{k}}$, and (e) QP corrections of bulk NbS₂ for all \mathbf{k} points of the coarse Wannier grid as a function of E_0 . The data points that belong to the Fermi-surface bands are colored according to their largest orbital character (cf. Fig. 2), and the dashed red line in panel (e) serves as a guide to the eye.

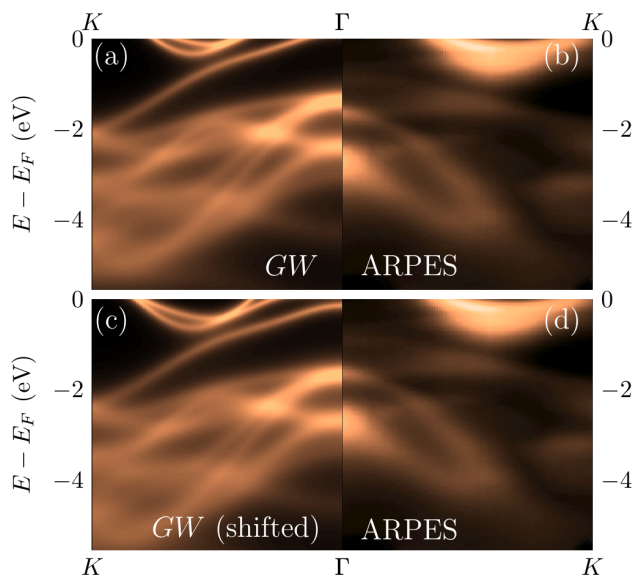


Figure 4. Comparison of the *GW* spectral function (a) of bulk NbS₂ with the ARPES measurements (b) from Ref. 35. The spectral functions have been calculated by broadening the QP energies with a Lorentzian of energy-dependent width. (c) *GW* spectral function shifted by 300 meV. (d) same as (b). Panels (b) and (d) are reprinted with permission from Ref. 35. Copyright (2016) by the American Physical Society.

to be recomputed, leading to additional complexity [57].

In the following, we want to take a detailed look at the changes of the Fermi surface, once *GW* corrections are taken into account. In Fig. 5 we illustrate the three sheets forming the Fermi surface: a disk-shaped pocket centered at the Γ point (S_{Γ_1}) originating from S p_z orbitals; another Γ centered, tube-shaped pocket (S_{Γ_2}) of Nb d_{z^2} character; and a K -centered, triangular-shaped pocket (S_K). The latter has Nb d_{z^2} character at the M point, but changes gradually to Nb d_{xy}/x^2-y^2 when moving along the surface. When electron-electron interactions are taken into account at the level of *GW* [Fig. 5(b)], S_{Γ_1} shrinks considerably, while S_{Γ_2} becomes more rounded and grows in diameter. Another impor-

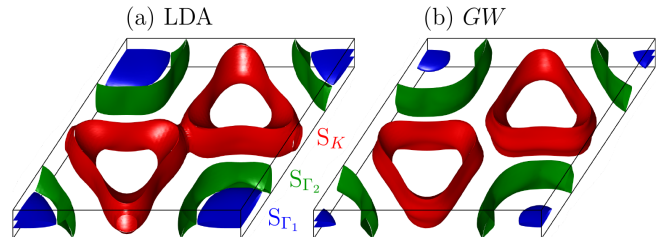


Figure 5. Fermi surfaces of bulk NbS₂ calculated within LDA (a) and *GW* (b), where the FS S_{Γ_1} is shown in blue, S_{Γ_2} in green and S_K in red. We want to stress that these colors do not represent the orbital contributions.

tant aspect of many-body corrections is the fact that the triangular S_K no longer extends up to the M point and it is no longer connected to the neighboring S_K Fermi surfaces.

In order to compare our Fermi surfaces with those from experiments, we broaden the QP energies close to the Fermi level by a Lorentzian with an energy-dependent width, as detailed before, to mimic the energy and momentum resolution of ARPES measurements (Fig. 6). As the experiments do not resolve the out-of-plane component, we also average over k_z . Independent of the method, the S_{Γ_1} Fermi surface is indiscernible from the background, in agreement with experiments [35], where the polarization of the incident beam probably has vanishing dipole matrix elements with the p_z orbitals, as mentioned before. Only the Nb d orbitals provide visible contributions to the Fermi surface, and due to the more rounded and disconnected S_K Fermi surface, the *GW* calculation yields a better agreement with ARPES measurements than the LDA. Again, by rigidly shifting our *GW* results by 300 meV, as shown in Fig. 6(c), we obtain very good agreement with experiments.

B. Monolayer NbS₂

We now want to focus our attention on the monolayer of NbS₂. In contrast to the bulk, the monolayer is comprised of only one formula unit, and due to the fact that

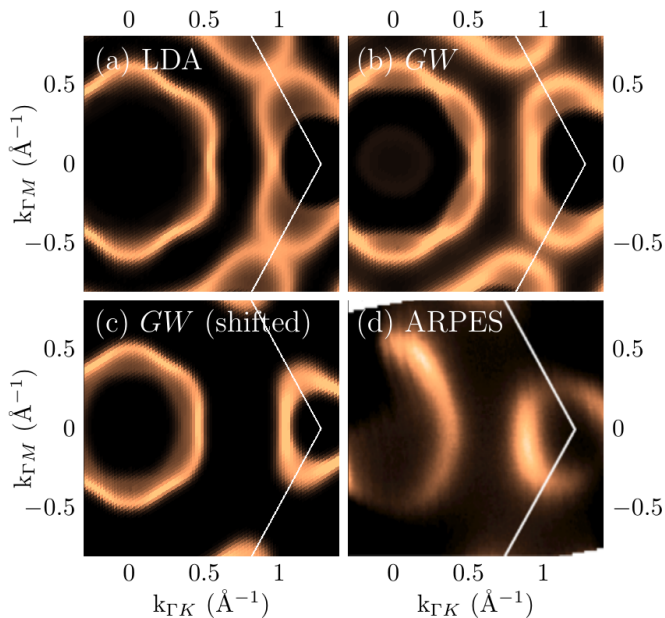


Figure 6. Fermi surfaces of bulk NbS₂ calculated within LDA (a) and *GW* (b), broadened with Lorentzians and averaged over k_z . In panel (c), we have shifted the Fermi level by 300 meV, corresponding to the electronic states shown in Fig. 4(c). For comparison with experiments, the measured ARPES Fermi surface from Ref. 35 is reproduced in panel (d). Panel (d) is reprinted with permission from Ref. 35. Copyright (2016) by the American Physical Society.

in the monolayer the interaction between neighboring S atoms along the z direction vanishes, the bandwidth of the S p_z states decreases, and they are pushed below the Fermi energy. The Fermi surface originates therefore from only one electron band, which has out-of-plane Nb d_{z^2} character around Γ and in-plane Nb d_{xy/x^2-y^2} character around K , as shown in Fig. 7. At the M point we find a mixture of these orbital contributions.

The impact of many-body corrections is much more pronounced in the free-standing monolayer than in the bulk system. As shown in Fig. 7 by the dotted blue line, the band width of the electronic state crossing the Fermi level increases significantly, from 1.28 eV (LDA) to 2.66 eV (*GW*) and the DOS at the Fermi energy decreases by more than a factor of 2, i.e., from 2.48 to 0.82 eV⁻¹.

The observed increase of *GW* corrections in the free-standing monolayer can be attributed to the fact that the Coulomb screening is weaker in two-dimensional systems compared to their three-dimensional counterparts. For the isolated monolayer, the electric-field lines close in the vacuum region, therefore increasing the screened Coulomb interaction, as has been reported for many different systems, including BN, MoS₂, and graphene [2, 15, 17–19, 70–74]. This effect is particularly important when comparing calculations with experiments where few-layer systems or monolayers are placed on substrates, which will influence the screening in the sample. In order to assess the effects of the sub-

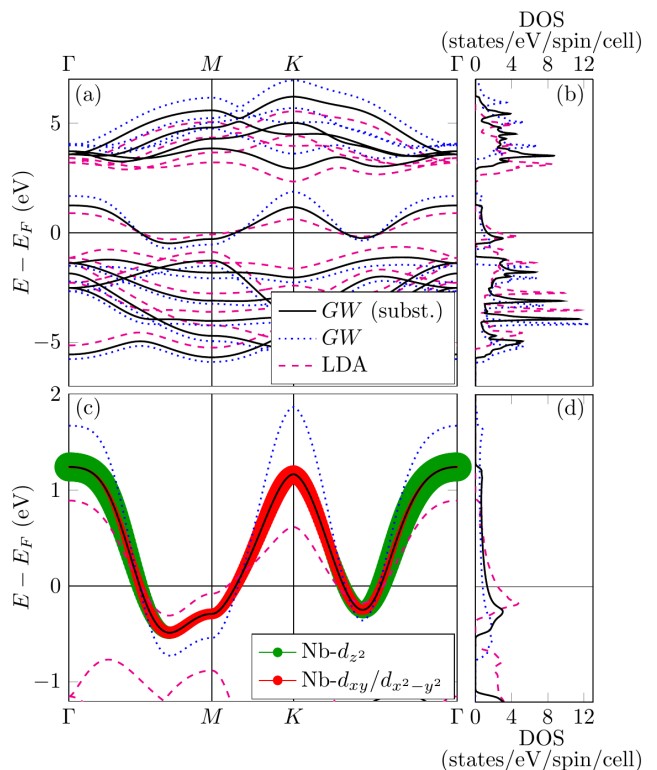


Figure 7. Comparison of the band structure (a), (c), and DOS (b), (d) of monolayer 2H-NbS₂ on the level of LDA (dashed magenta) and with *GW* renormalization, neglecting and including substrate effects (solid black and dotted blue lines, respectively). In (c), the orbital contributions of the out-of-plane Nb d_{z^2} and in-plane Nb d_{xy/x^2-y^2} are given by the size of the colored markers in green and red, respectively.

strate, we performed an additional *GW* calculation for the monolayer of NbS₂, where we incorporated this effect by considering a semi-infinite medium of dielectric constant ϵ_S on one side of the monolayer, and vacuum on the other [15]. As we are not aware of any experimental work on monolayer NbS₂, we chose $\epsilon_S = 4$, which is a good approximation for the dielectric constants of the substrates usually used when performing measurements on monolayer NbSe₂, such as SiC and hexagonal BN [23, 75–78].

The results of this calculation are shown as solid black lines in Fig. 7, where one can observe a considerable reduction of the *GW* corrections. This becomes even more apparent when looking at V_{xc} , Σ_x , $\text{Re}[\Sigma_c(E_0)]$, $Z_{n,\mathbf{k}}$, and the QP corrections, as provided in Fig. 8, where the results of the calculations with (without) substrate are shown as circles (squares). The overall behavior of these quantities as a function of the respective DFT eigenvalues is very similar to the bulk case, i.e., V_{xc} is in good approximation linearly decreasing with increasing E_0 , while Σ_x is increasing with a steep slope for values close to E_F , closely following the trend of a homogeneous electron gas [66]. The reverse trend of Σ_x is found for

$\text{Re}[\Sigma_c(E_0)]$. The QP strength $Z_{n,\mathbf{k}}$ is larger in both cases as compared to bulk. In particular, taking substrate effects into account leads to high QP strengths from 0.87 to 0.93, which correspond to Fermi velocity renormalizations around -9% . In contrast to the bulk, there is a marked change in the slope around the Fermi level in the *GW* quasiparticle corrections when plotted as function of the LDA eigenvalues, as shown in Fig. 8(e). We ascribe this behavior to the fact that the Coulomb interaction is significantly larger compared to the bulk due to the reduced electronic screening. We want to mention at this point that our calculations for monolayer NbS_2 are in good agreement with those presented in Ref. 34 for monolayer NbSe_2 . In general, we observe that the many-body corrections in NbS_2 are larger than in NbSe_2 , but they follow the same trend, i.e., a decrease of the quasiparticle energy around the *M* point, and an increase around Γ and *K*. Also, the Fermi surfaces become more rounded and circular in both materials due to the inclusion of *GW* corrections.

Using a Lorentzian with energy-dependent broadening to simulate the experimental resolution, we provide a prediction for the ARPES spectrum of monolayer NbS_2 in Fig. 9. There, we show the energy-resolved spectral function along the Γ -*K* high-symmetry direction, and compare the results for the monolayer on a substrate and without. The ratio of the effective mass m_{GW}/m_{LDA} of the Fermi-surface band shown in Fig. 9 increases from 0.3 to 0.5 when substrate effects are taken into account.

In Fig. 10, we provide our prediction for the Fermi surface of a monolayer of NbS_2 . While the LDA Fermi surface exhibits triangular-shaped, *K*-centered sheets that are almost connected to each other, the *GW* calculations show more circular, disconnected pockets. In general, the features of the *GW* Fermi surface are clearer due to the steeper electron bands around the Fermi level. The Fermi surface does not change when comparing the free-standing monolayer with the monolayer on a substrate.

IV. CONCLUSIONS

In this work, we employed the Sternheimer*GW* method to perform a detailed investigation of the electronic properties of bulk and monolayer NbS_2 , using many-body perturbation theory in the framework of the *GW* approximation. We document in the appendixes convergence studies for the *GW* calculations, to serve as a solid technical foundation for future investigations including many-body corrections in metallic transition-metal dichalcogenides.

We analyzed the individual components of the self-energy, and found that Σ_x behaves as in the homogeneous electron gas. The QP strength is found to be between 0.54 and 0.74 for the bulk, and between 0.87 and 0.93 for the monolayer (when we take into account substrate screening).

For the bulk system, we find that the inclusion of many-body corrections increases the bandwidth of the

S p and *Nb d* bands by pushing the unoccupied states to higher energies, and a decrease of the DOS at the Fermi level by 18%. This decrease of the DOS has important effects on the electron-phonon coupling and superconductivity in this compound. In addition, we have compared our calculations with ARPES measurements and found that including many-body effects improves the agreement between theory and experiments in terms of the shape of the Fermi surface and the low-energy electronic structure. We also observe that a Fermi-level shift of 300 meV brings our calculations in very good agreement with the ARPES measurements. We proposed that such a shift could arise from unintentional doping in the experimental sample.

For the monolayer system, we observe a strong increase of the screened Coulomb interaction as compared to bulk due to its two-dimensional nature, and we have shown that the consideration of a substrate via changing the dielectric constant on one side of the monolayer results in a marked reduction of the interaction potential and the effects of the many-body corrections. When we take into account the screening from the substrate, the electronic bandwidth is smaller than in the free-standing case, and the DOS at the Fermi level is larger. This in turn also means that the electron-phonon coupling and superconducting properties will be sensitive to the choice of substrate. As another example of the importance of substrate effects, we find that the ratio of the effective masses is 1.7 times larger for the NbS_2 monolayer on a substrate compared to the free-standing monolayer. As we are not aware of any experimental work on monolayer NbS_2 , these calculations provide a first insight into the electronic properties of this compound beyond DFT.

In summary, this work highlights the importance to include many-body perturbation theory corrections in the study of metallic TMDs. These corrections will lead to improved carrier velocities and densities of states, and are crucial for a more accurate understanding of charge transport and superconductivity in these compounds.

ACKNOWLEDGMENTS

We are grateful to Professor N. Mannella and the other authors of Ref. 35 for the permission to use their ARPES results for comparison with our data, and we acknowledge fruitful discussions with G. Volonakis and N. Zibouche. This work was supported by the Austrian Science Fund (FWF) Project No. J 3806-N36, the Leverhulme Trust (Grant No. RL-2012-001), the UK Engineering and Physical Sciences Research Council (Grant No. EP/M020517/1), the Graphene Flagship (Horizon 2020 Grant No. 785219 - GrapheneCore2), the University of Oxford Advanced Research Computing (ARC) facility (<http://dx.doi.org/810.5281/zenodo.22558>), the ARCHER UK National Supercomputing Service under the ‘AMSEC’ Leadership project, the Vienna Scientific Cluster (VSC), and the Cambridge Service for

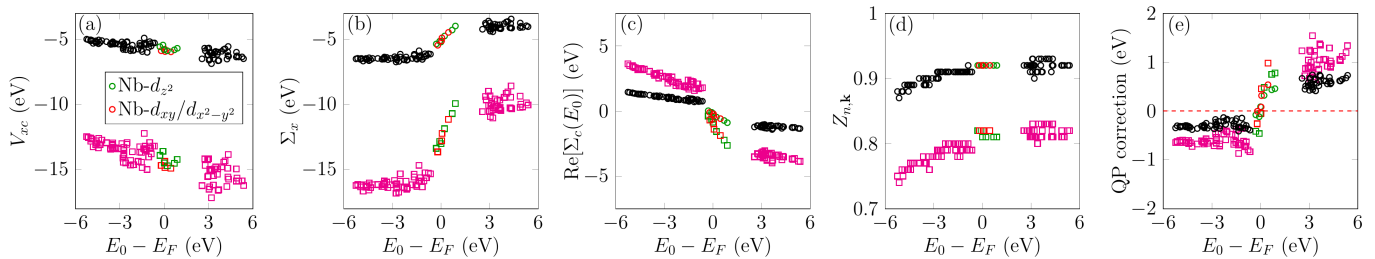


Figure 8. (a) Exchange-correlation potential V_{xc} , (b) exchange-part Σ_x of the self-energy, (c) real part of the correlation self-energy Σ_c at the DFT eigenvalues E_0 , (d) QP renormalization factor $Z_{n,\mathbf{k}}$, and (e) QP corrections of monolayer NbS₂ for all \mathbf{k} points of the coarse Wannier grid as a function of E_0 for the free-standing monolayer (squares) and with considered substrate (circles). The data points that belong to the Fermi-surface bands have been colored according to their largest orbital character (cf. Fig. 7), and the dashed red line in panel (e) serves as a guide to the eye.

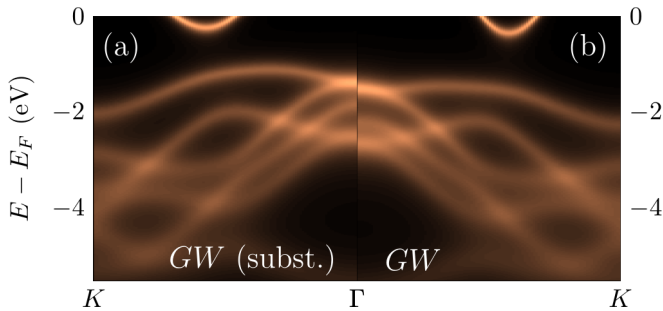


Figure 9. Spectral function for a monolayer of NbS₂ with (left) and without (right) substrate, along the high-symmetry Γ - K path. The GW quasiparticle peaks are broadened using Lorentzians of energy-dependent width.

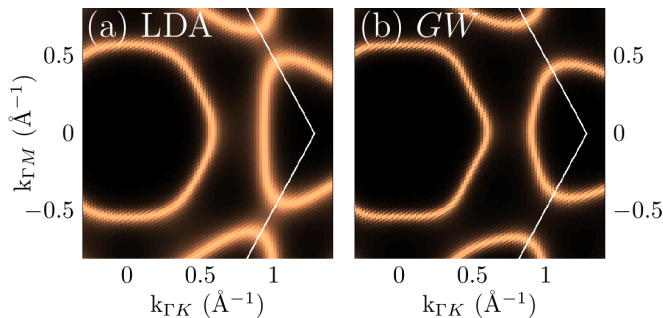


Figure 10. Fermi surfaces for monolayer NbS₂, calculated within LDA (a) and GW (b), where the band structure has been broadened with Lorentzians. The effects of a substrate on the GW Fermi surface are negligible (not shown).

Data Driven Discovery (CSD3) funded by EPSRC (grant EP/P020259/1). We further acknowledge PRACE for awarding us access to Cartesius at SURFsara, Netherlands; Abel at UiO, Norway, and MareNostrum at BSC-CNS, Spain.

Appendix A: Effect of SOC

In Figs. 11 and 12 we provide a comparison of the DFT band structure with (dashed blue) and without (solid red) SOC for bulk and monolayer NbS₂, respectively. For these calculations, fully relativistic optimized norm-conserving Vanderbilt pseudopotentials [79, 80] within PZ [62] that include the semi-core electrons of Nb have been used. As one can see, SOC leads to band splittings around the K point. For the bulk, we calculate a splitting of ~ 74 meV and for the free-standing monolayer a splitting of ~ 52 meV. These values are within the accuracy of our GW results, and are therefore neglected.

Appendix B: Effect of van der Waals corrections

In this appendix we discuss the effects of including van der Waals corrections on the band structure of bulk NbS₂. In Fig. 13, we show as solid black lines the band structure at the level of GW without considering vdW effects, while for the dashed magenta line we have included vdW interactions according to the semiempirical Grimme D2 corrections [81]. As can be appreciated in this figure, the changes to the band structure are small, and the DOS in the low-energy range is almost identical. The most marked difference is the fact that with vdW corrections, the $S p_z$ close to the Γ point falls below the Fermi energy.

This can also be observed in Fig. 14, where we show the GW spectral function with and without vdW corrections during the structure optimization. Apart from the QP band coming from $S p_z$ states, the two spectral functions are almost indistinguishable.

Moving on to the Fermi surfaces shown in Fig. 15, we find that, apart from very small, the structure optimized with vdW corrections leads to very similar results for the GW spectral function at low energies.

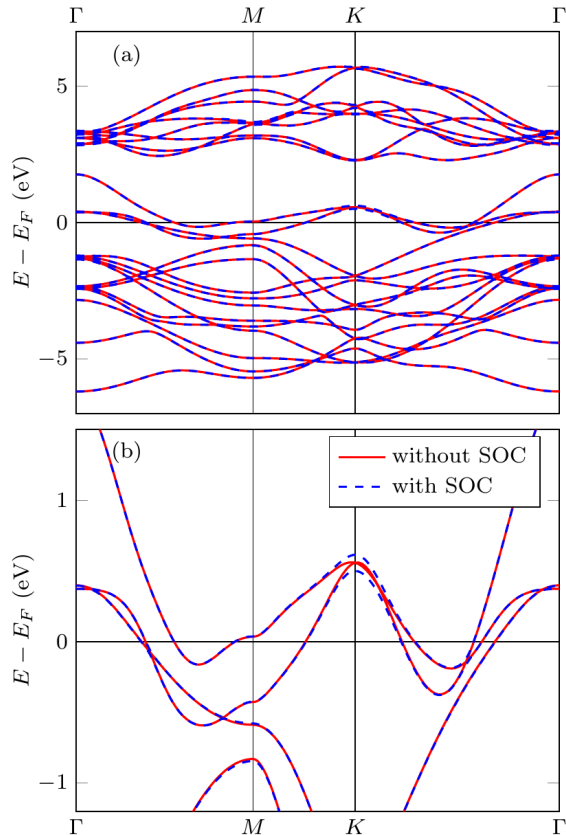


Figure 11. Comparison of the LDA band structure of bulk NbS₂ with (dashed, blue) and without (solid red) SOC. Panel (b) is a zoom of (a).

Appendix C: Convergence studies for bulk NbS₂

1. Plane wave cutoff for ground state DFT calculations

First, we test the convergence of our *GW* calculations with respect to the kinetic-energy cutoff E_k for the plane waves used in the ground-state DFT calculation. We report the results of this study in Table I, where we show the inverse of the diagonal element of the dielectric matrix $\epsilon_i = \epsilon_{\mathbf{G}_i, \mathbf{G}_i}(\mathbf{q}, \omega)$ with $\mathbf{G}_i = (i, 0, 0)2\pi/a$, evaluated at $\mathbf{q} = \Gamma$ and $\omega = 0$.

In Table II, we show the values of Σ_x of the four QP states at Γ closest to the Fermi level as a function of the cutoff value. As one can see, our target accuracy of < 100 meV is already met for 30 Ry. The maximum deviation falls below 30 meV for a cutoff of 40 Ry.

2. Brillouin zone sampling

In SternheimerGW, there are three BZ grids to consider: (i) the grid used to sample the exchange, (ii) the grid used to sample the correlation, and (iii) the grid

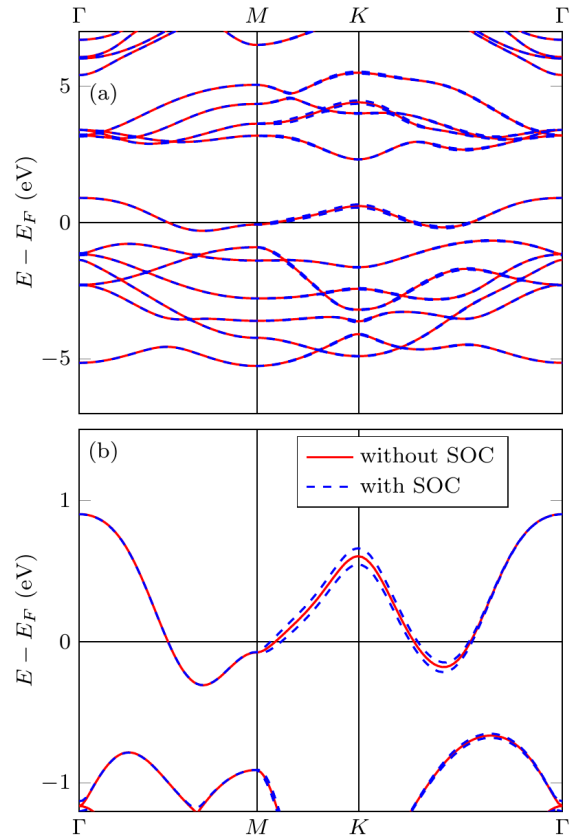


Figure 12. Comparison of the LDA band structure of the free-standing NbS₂ monolayer with (dashed, blue) and without (solid red) SOC. Panel (b) is a zoom of (a).

Table I. The inverse of $\epsilon_i = \epsilon_{\mathbf{G}_i, \mathbf{G}_i}(\mathbf{q}, \omega)$ with $\mathbf{G}_i = (i, 0, 0)2\pi/a$, evaluated at $\mathbf{q} = \Gamma$ and $\omega = 0$, as a function of the kinetic-energy cutoff E_k for the plane waves of the DFT ground-state calculation. For these calculations, we used an $8 \times 8 \times 4$ \mathbf{k} grid, an energy cutoff in the dielectric matrix of 10 Ry, and an energy cutoff of 20 Ry in the exchange part of the self-energy.

E_k (Ry)	$1/\epsilon_2$	$1/\epsilon_3$	$1/\epsilon_4$
30	0.049	0.192	0.335
40	0.045	0.188	0.328
50	0.046	0.188	0.329
60	0.046	0.188	0.329
70	0.046	0.188	0.329

used to sample the dielectric response (in our calculations, this grid is set to be the same as for the exchange). The dependence of the correlation part of the self-energy on the number of points used to sample the Brillouin zone is shown in Fig. 16, where we plot the inverse of the first four diagonal elements of $\epsilon_i = \epsilon_{\mathbf{G}_i, \mathbf{G}_i}(\mathbf{q}, \omega)$ with $\mathbf{G}_i = (i, 0, 0)2\pi/a$ evaluated at $\mathbf{q} = \Gamma$ and $\omega = 0$.

While the convergence of the correlation part is quite

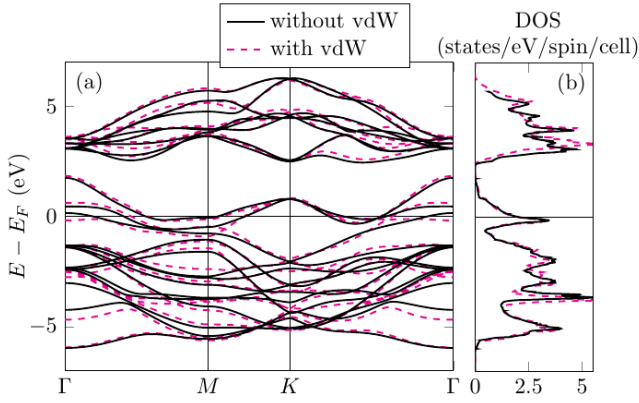


Figure 13. Band structure of bulk NbS₂ with included *GW* corrections, where the structure has been optimized at the DFT level with (dashed, magenta) and without (black, solid) van der Waals corrections.

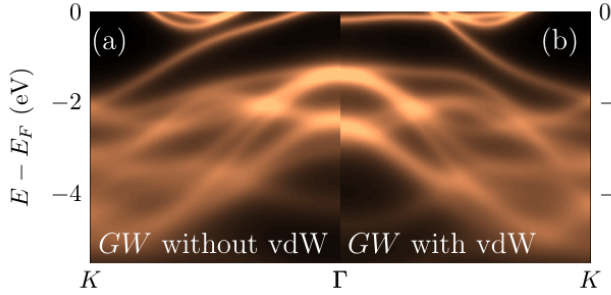


Figure 14. Comparison of the *GW* spectral function of bulk NbS₂ (a) without and (b) with vdW corrections during the structure optimization. The spectral functions have been calculated by broadening the QP energies with a Lorentzian of energy-dependent width, as in Fig. 4.

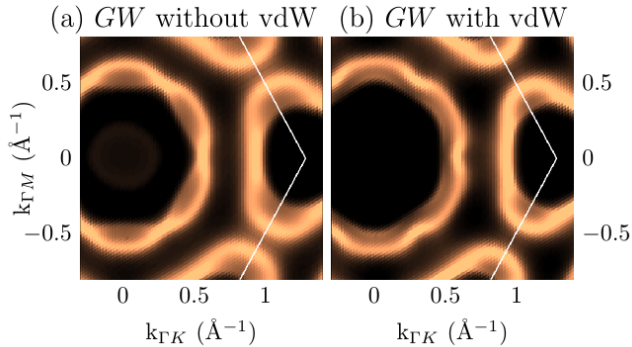


Figure 15. *GW* Fermi surfaces of bulk NbS₂ calculated (a) without and (b) with van der Waals corrections during the structure optimization. The spectral functions have been calculated by broadening the QP energies with a Lorentzian of energy-dependent width, as in Fig. 6.

Table II. $\Sigma_x(\mathbf{k})$ of the four electronic states closest to the Fermi energy at $\mathbf{k} = \Gamma$ (at the DFT level) as a function of the kinetic-energy cutoff E_k for the plane waves of the DFT ground-state calculation. For these calculations, we used an $8 \times 8 \times 4$ \mathbf{k} grid, an energy cutoff in the dielectric matrix of 10 Ry, and an energy cutoff of 20 Ry in the exchange part of the self-energy.

E_k (Ry)	band 1 (eV)	band 2 (eV)	band 3 (eV)	band 4 (eV)
30	-16.83	-11.61	-13.70	-10.77
40	-16.82	-11.55	-13.73	-10.72
50	-16.82	-11.52	-13.75	-10.71
60	-16.81	-11.51	-13.75	-10.70
70	-16.82	-11.51	-13.75	-10.70

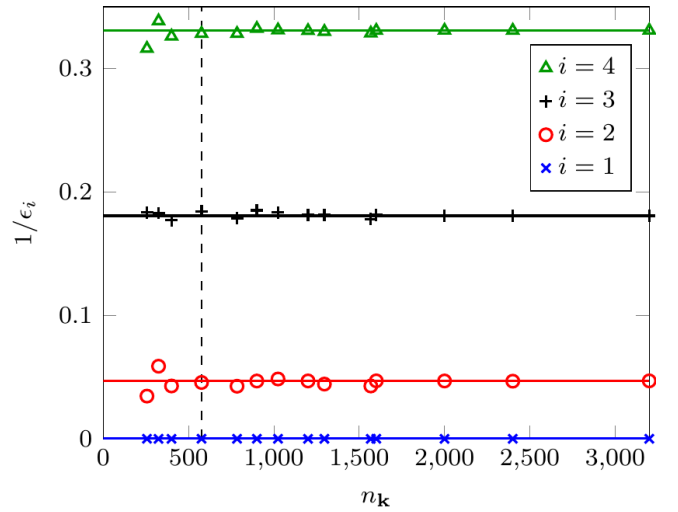


Figure 16. The inverse of the first four diagonal elements of $\epsilon_i = \epsilon_{\mathbf{G}_i, \mathbf{G}_i}(\mathbf{q}, \omega)$ with $\mathbf{G}_i = (i, 0, 0)2\pi/a$, evaluated at $\mathbf{q} = \Gamma$ and $\omega = 0$, as a function of the number of \mathbf{k} points. The vertical dashed line indicates the value for the $12 \times 12 \times 4$ BZ grid used in the final calculations.

smooth, the exchange part of the self-energy is more difficult to converge with respect to the number of BZ points. We notice that achieving convergence for the two bands closest to the Fermi level is particularly difficult, while the convergence of the other states is very fast. In Fig. 17 we show Σ_x at Γ as a function of the number of BZ points $n_{\mathbf{k}}$, where we have connected with a blue line those points that have a common $n_{\mathbf{k}_{x,y}}/n_{\mathbf{k}_z} = 3$ ratio, similar to the lattice vector lengths' ratio. The vertical dashed lines indicate the values for a $27 \times 27 \times 9$ BZ grid, which we consider converged. The large deviations between single points and the bulging downwards of the blue curve are largely due to finite-size effects coming from the \mathbf{k}_z sampling. As calculations for a $27 \times 27 \times 9$ grid are at the moment not feasible, we chose a $12 \times 12 \times 4$ grid that allows for reasonably fast calculations while still maintaining an accuracy of < 100 meV relative to the $27 \times 27 \times 9$ grid.

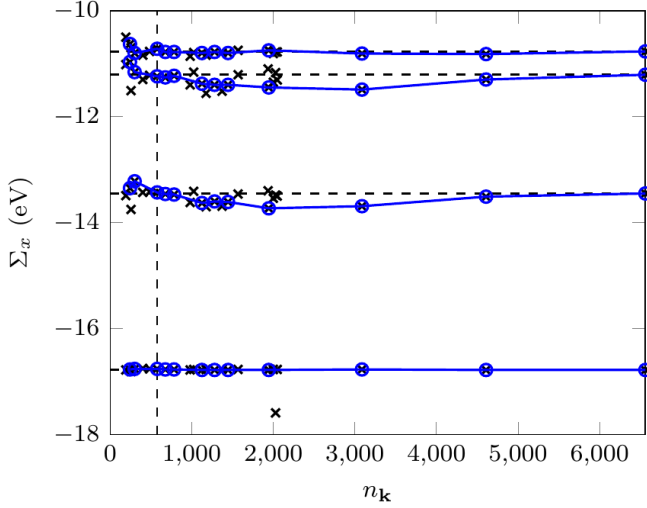


Figure 17. Σ_x at Γ of the four electronic states closest to the Fermi energy (at DFT level) as a function of the number of BZ grid points. The vertical dashed line indicates the value for the $12 \times 12 \times 4$ \mathbf{k} grid used in the final calculations. Data points that have a common ratio $n_{\mathbf{k}_{x,y}}/n_{\mathbf{k}_z} = 3$ are connected with a blue line.

3. Energy cutoff E_c for the correlation part of the self-energy Σ_c

In Table III we report the convergence of the diagonal elements of the screened Coulomb interaction matrix $W_i = W_{\mathbf{G}_i, \mathbf{G}_i}(\mathbf{q}, \omega)$ with $\mathbf{G}_i = (i, 0, 0)2\pi/a$, evaluated at $\mathbf{q} = \Gamma$ and $\omega = 0$, as a function of the energy cutoff E_c of the dielectric matrix.

Table III. Diagonal elements of the screened Coulomb interaction $W_i = W_{\mathbf{G}_i, \mathbf{G}_i}(\mathbf{q}, \omega)$ with $\mathbf{G}_i = (i, 0, 0)2\pi/a$, evaluated at $\mathbf{q} = \Gamma$ and $\omega = 0$, as a function of the energy cutoff E_c for the dielectric matrix. For these calculations, we used an $8 \times 8 \times 4$ \mathbf{k} grid and a plane-wave cutoff of 40 Ry.

E_c (Ry)	W_2	W_4	W_{10}	W_{14}
6	-0.9013	-0.6964	-0.5344	-0.5071
8	-0.9010	-0.6961	-0.5337	-0.5066
10	-0.9008	-0.6950	-0.5334	-0.5065
12	-0.9006	-0.6944	-0.5333	-0.5064
14	-0.9006	-0.6940	-0.5335	-0.5063
16	-0.9005	-0.6936	-0.5331	-0.5064

In Table IV we show the convergence behavior of the GW quasiparticle energies at Γ closest to the DFT Fermi energy as a function of the energy cutoff E_c for the dielectric matrix. The convergence is relatively fast, allowing us to choose a value of 10 Ry for all subsequent calculations

Table IV. Quasiparticle eigenvalues of the four electronic states at Γ closest to the Fermi energy (at DFT level) as a function of the energy cutoff E_c for the dielectric matrix. For these calculations, we used an $8 \times 8 \times 4$ \mathbf{k} grid, a plane-wave cutoff of 40 Ry, and an energy cutoff for the exchange part of 20 Ry.

E_c (Ry)	band 1 (eV)	band 2 (eV)	band 3 (eV)	band 4 (eV)
6	7.67	14.26	11.61	16.56
8	8.28	9.47	10.78	12.00
10	8.27	9.43	10.56	11.70
12	8.24	9.39	10.40	11.54
14	8.20	9.36	10.31	11.44
16	8.19	9.34	10.26	11.41

4. Energy cutoff E_x for the exchange part of the self-energy Σ_x

In order to test the dependence of our results on the energy cutoff E_x of the exchange part of the self-energy, we again inspected its values for electronic states closest to the Fermi level at the Γ point (see Table V). While the deviations between calculations with cutoffs of 20 and 35 Ry are larger than 100 meV for three of the bands, these discrepancies are reduced to < 50 meV if a cutoff of 25 Ry is chosen.

Table V. $\Sigma_x(\mathbf{k})$ of the four electronic states at Γ closest to the Fermi energy (at DFT level) as a function of the energy cutoff E_x . For these calculations, we used an $8 \times 8 \times 4$ \mathbf{k} grid, an energy cutoff in the dielectric matrix of 10 Ry, and a plane-wave cutoff of 40 Ry.

E_x	band 1 (eV)	band 2 (eV)	band 3 (eV)	band 4 (eV)
20	-16.81	-11.51	-13.75	-10.70
25	-16.88	-11.61	-13.77	-10.80
30	-16.90	-11.65	-13.78	-10.84
35	-16.91	-11.66	-13.78	-10.85

Appendix D: Convergence studies for monolayer NbS₂

1. Plane wave cutoff for ground state DFT calculations

In Table VI we report the convergence of the diagonal elements of the screened Coulomb interaction $W_i = W_{\mathbf{G}_i, \mathbf{G}_i}(\mathbf{q}, \omega)$ with $\mathbf{G}_i = (i, 0, 0)2\pi/a$, evaluated at $\mathbf{q} = \Gamma$ and $\omega = 0$, as a function of the kinetic-energy cutoff E_k for the plane waves of the DFT ground-state calculation, and in Table VII the convergence of $\Sigma_x(\mathbf{k})$ for the three electronic states at $\mathbf{k} = \Gamma$ closest to the Fermi energy. The convergence with respect to the kinetic-energy cut-

off is quite fast, allowing us to choose a value of 40 Ry to achieve an accuracy < 100 meV.

Table VI. The screened Coulomb interaction $W_i = W_{\mathbf{G}_i, \mathbf{G}_i}(\mathbf{q}, \omega)$ with $\mathbf{G}_i = (i, 0, 0)2\pi/a$, evaluated at $\mathbf{q} = \Gamma$ and $\omega = 0$, as a function of the kinetic energy cutoff E_k for the plane waves of the DFT ground state calculation. For these calculations, we used a $24 \times 24 \times 1$ \mathbf{k} -grid, an energy cutoff in the dielectric matrix of 10 Ry and an energy cutoff of 20 Ry in the exchange part of the self-energy.

E_k (Ry)	W_2	W_4	W_6
20	-0.6721	-0.2595	-0.2423
30	-0.6741	-0.2600	-0.2433
40	-0.6737	-0.2598	-0.2430
50	-0.6735	-0.2598	-0.2429
60	-0.6734	-0.2597	-0.2428

Table VII. $\Sigma_x(\mathbf{k})$ of the three electronic states at $\mathbf{k} = \Gamma$ closest to the Fermi energy (at DFT level) as a function of the kinetic energy cutoff E_k for the plane-waves of the DFT ground state calculation. For these calculations, we used a $12 \times 12 \times 1$ \mathbf{k} grid and an energy cutoff in the dielectric matrix of 10 Ry.

E_k (Ry)	band 1 (eV)	band 2 (eV)	band 3 (eV)
20	-16.03	-9.82	-10.29
30	-16.04	-9.87	-10.34
40	-16.03	-9.84	-10.30
50	-16.02	-9.82	-10.29
60	-16.02	-9.81	-10.28

2. Brillouin zone sampling

In Table VIII we report the convergence of diagonal elements of the screened Coulomb interaction $W_i = W_{\mathbf{G}_i, \mathbf{G}_i}(\mathbf{q}, \omega)$ with $\mathbf{G}_i = (i, 0, 0)2\pi/a$, evaluated at $\mathbf{q} = \Gamma$ and $\omega = 0$, as a function of the number of BZ points $n_{\mathbf{k}}$ used to sample the Brillouin zone, which shows a very favorable behavior. Converging the exchange part of the self-energy with respect to the number of BZ points is less smooth than for the correlation part, as already noticed for the bulk. In contrast to the bulk, however, we find that the slowest convergence is not observed for the state crossing the Fermi level, but for the fully occupied band below, as can be seen in Fig. 18. The difference in $\Sigma_x(\mathbf{k} = \Gamma)$ for this electronic state between the chosen $24 \times 24 \times 1$ BZ grid and a $44 \times 44 \times 1$ grid, considered converged, is around 200 meV. As this electronic band is fully occupied and will only be pushed further down in energy, the Fermi surface, which is our main point of focus, will not change and we accept a larger inaccuracy for this state in view of reducing computational time.

Table VIII. Diagonal elements of the screened Coulomb interaction $W_i = W_{\mathbf{G}_i, \mathbf{G}_i}(\mathbf{q}, \omega)$ with $\mathbf{G}_i = (i, 0, 0)2\pi/a$, evaluated at $\mathbf{q} = \Gamma$ and $\omega = 0$, as a function of the number of BZ-points $n_{\mathbf{k}}$ used to sample the Brillouin zone. For these calculations, we used an energy cutoff in the dielectric matrix of 10 Ry and an energy cutoff of 20 Ry in the exchange part of the self-energy.

$n_{\mathbf{k}}$ (Ry)	W_2	W_4	W_6
8^2	-0.6788	-0.2600	-0.2431
12^2	-0.6711	-0.2596	-0.2429
16^2	-0.6723	-0.2597	-0.2430
20^2	-0.6736	-0.2598	-0.2430
24^2	-0.6737	-0.2598	-0.2430
28^2	-0.6737	-0.2599	-0.2430
32^2	-0.6738	-0.2599	-0.2430
36^2	-0.6738	-0.2599	-0.2430

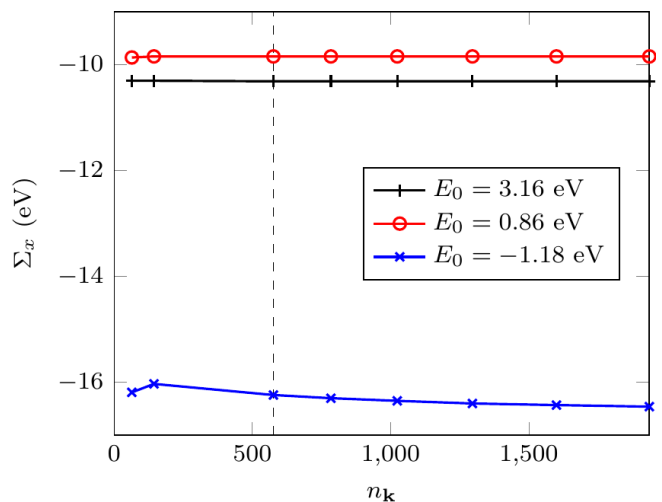


Figure 18. $\Sigma_x(\mathbf{k})$ of the three electronic states at $\mathbf{k} = \Gamma$ closest to the Fermi energy (at DFT level) as a function of the number of BZ points $n_{\mathbf{k}}$. The vertical dashed line indicates the value for the $24 \times 24 \times 1$ BZ grid used in the final calculations.

3. Energy cutoff E_c for the correlation part of the self-energy Σ_c

In Table IX we report the convergence of diagonal elements of the screened Coulomb interaction $W_i = W_{\mathbf{G}_i, \mathbf{G}_i}(\mathbf{q}, \omega)$ with $\mathbf{G}_i = (i, 0, 0)2\pi/a$ evaluated at $\mathbf{q} = \Gamma$ and $\omega = 0$ as a function of the energy cutoff E_c for the dielectric matrix.

In Table X we show the convergence behavior of the GW quasiparticle energies at Γ closest to the DFT Fermi energy as a function of the energy cutoff E_c for the dielectric matrix. Convergence is very fast, allowing us to choose a value of 10 Ry for the energy cutoff E_c .

Table IX. Diagonal elements of the screened Coulomb interaction $W_i = W_{\mathbf{G}_i, \mathbf{G}_i}(\mathbf{q}, \omega)$ with $\mathbf{G}_i = (i, 0, 0)2\pi/a$, evaluated at $\mathbf{q} = \Gamma$ and $\omega = 0$, as a function of the energy cutoff E_c for the dielectric matrix. For these calculations, we used a $24 \times 24 \times 1$ \mathbf{k} grid and a plane-wave cutoff of 40 Ry.

E_c (Ry)	W_2	W_4	W_6
6	-0.6575	-0.2487	-0.2043
8	-0.6571	-0.2485	-0.2042
10	-0.6569	-0.2484	-0.2041
12	-0.6568	-0.2484	-0.2041
14	-0.6568	-0.2484	-0.2041

Table X. Quasiparticle eigenvalues of the three electronic states at Γ closest to the Fermi energy (at DFT level) as a function of the energy cutoff E_c for the dielectric matrix. For these calculations, we used an $12 \times 12 \times 1$ \mathbf{k} grid, a plane-wave cutoff of 40 Ry, and an energy cutoff for the exchange part of 20 Ry.

E_c (Ry)	band 1 (eV)	band 2 (eV)	band 3 (eV)
6	-2.77	0.89	3.29
8	-2.78	0.65	2.93
10	-2.81	0.44	2.71
12	-2.87	0.30	2.57
14	-2.92	0.19	2.46
16	-2.94	0.16	2.42

4. Energy cutoff E_x for the exchange part of the self-energy Σ_x

In Table XI we report the convergence of $\Sigma_x(\mathbf{k})$ of the three electronic states at Γ closest to the Fermi energy (at DFT level) as a function of the energy cutoff E_x . We find again that not the electronic state crossing the Fermi level, but the one below, shows the slowest convergence. Still, by choosing $E_x = 25$ Ry, we can achieve an accuracy of < 50 meV.

Table XI. $\Sigma_x(\mathbf{k})$ of the three electronic states at $\mathbf{k} = \Gamma$ closest to the Fermi energy (at DFT level) as a function of the energy cutoff E_x . For these calculations, we used a $12 \times 12 \times 1$ \mathbf{k} -grid, an energy cutoff in the dielectric matrix of 10 Ry and a plane wave cutoff of 40 Ry.

E_x	band 1 (eV)	band 2 (eV)	band 3 (eV)
15	-15.80	-9.47	-9.97
20	-16.03	-9.84	-10.30
25	-16.11	-9.93	-10.40
30	-16.14	-9.96	-10.43
35	-16.14	-9.97	-10.44

* feliciano.giustino@materials.ox.ac.uk

¹ B. Sipos, A. F. Kusmartseva, A. Akrap, H. Berger, L. Forró, and E. Tutiš, *Nat. Mater* **7**, 960 (2008).

² Q. H. Wang, K. Kalantar-Zadeh, A. Kis, J. N. Coleman, and M. S. Strano, *Nat. Nano* **7**, 699 (2012).

³ A. K. Geim and I. V. Grigorieva, *Nature (London)* **499**, 419 (2013).

⁴ S. Manzeli, D. Ovchinnikov, D. Pasquier, O. V. Yazyev, and A. Kis, *Nat. Rev. Mater.* **2**, 201733 (2017).

⁵ J. Wilson and A. Yoffe, *Adv. Phys* **18**, 193 (1969).

⁶ D. E. Moncton, J. D. Axe, and F. J. DiSalvo, *Phys. Rev. Lett.* **34**, 734 (1975).

⁷ T. Valla, A. V. Fedorov, P. D. Johnson, P.-A. Glans, C. McGuinness, K. E. Smith, E. Y. Andrei, and H. Berger, *Phys. Rev. Lett.* **92**, 086401 (2004).

⁸ F. Weber, S. Rosenkranz, J.-P. Castellán, R. Osborn, R. Hott, R. Heid, K.-P. Bohnen, T. Egami, A. H. Said, and D. Reznik, *Phys. Rev. Lett.* **107**, 107403 (2011).

⁹ M. Calandra and F. Mauri, *Phys. Rev. Lett.* **106**, 196406 (2011).

¹⁰ M. Rösner, S. Haas, and T. O. Wehling, *Phys. Rev. B* **90**, 245105 (2014).

¹¹ M. Leroux, I. Errea, M. Le Tacon, S.-M. Souliou, G. Garbarino, L. Cario, A. Bosak, F. Mauri, M. Calandra, and P. Rodière, *Phys. Rev. B* **92**, 140303 (2015).

- ¹² T. Das and K. Dolui, *Phys. Rev. B* **91**, 094510 (2015).
- ¹³ R. A. Klemm, *Physica C* **514**, 86 (2015).
- ¹⁴ Y. Ding, Y. Wang, J. Ni, L. Shi, S. Shi, and W. Tang, *Physica B: Condensed Matter* **406**, 2254 (2011).
- ¹⁵ C.-H. Park, F. Giustino, C. D. Spataru, M. L. Cohen, and S. G. Louie, *Phys. Rev. Lett.* **102**, 076803 (2009).
- ¹⁶ S. Das Sarma, S. Adam, E. H. Hwang, and E. Rossi, *Rev. Mod. Phys.* **83**, 407 (2011).
- ¹⁷ V. N. Kotov, B. Uchoa, V. M. Pereira, F. Guinea, and A. H. Castro Neto, *Rev. Mod. Phys.* **84**, 1067 (2012).
- ¹⁸ D. Y. Qiu, F. H. da Jornada, and S. G. Louie, *Phys. Rev. Lett.* **111**, 216805 (2013).
- ¹⁹ M. M. Ugeda, A. J. Bradley, S.-F. Shi, F. H. d. Jornada, Y. Zhang, D. Y. Qiu, W. Ruan, S.-K. Mo, Z. Hussain, Z.-X. Shen, F. Wang, S. G. Louie, and M. F. Crommie, *Nat. Mater* **13**, 1091 (2014).
- ²⁰ Y. Yu, F. Yang, X. F. Lu, Y. J. Yan, Y.-H. Cho, L. Ma, X. Niu, S. Kim, Y.-W. Son, D. Feng, S. Li, S.-W. Cheong, X. H. Chen, and Y. Zhang, *Nat. Nanotechnol* **10**, 270 (2015).
- ²¹ M. M. Ugeda, A. J. Bradley, Y. Zhang, S. Onishi, Y. Chen, W. Ruan, C. Ojeda-Aristizabal, H. Ryu, M. T. Edmonds, H.-Z. Tsai, A. Riss, S.-K. Mo, D. Lee, A. Zettl, Z. Hussain, Z.-X. Shen, and M. F. Crommie, *Nat. Phys* **12**, 92 (2016).
- ²² K. Sugawara, Y. Nakata, R. Shimizu, P. Han, T. Hitosugi, T. Sato, and T. Takahashi, *ACS Nano* **10**, 1341 (2016).
- ²³ Y. Cao, A. Mishchenko, G. L. Yu, E. Khestanova, A. P. Rooney, E. Prestat, A. V. Kretinin, P. Blake, M. B. Shalom, C. Woods, J. Chapman, G. Balakrishnan, I. V. Grigorieva, K. S. Novoselov, B. A. Piot, M. Potemski, K. Watanabe, T. Taniguchi, S. J. Haigh, A. K. Geim, and R. V. Gorbachev, *Nano Lett.* **15**, 4914 (2015).
- ²⁴ X. Xi, L. Zhao, Z. Wang, H. Berger, L. Forró, J. Shan, and K. F. Mak, *Nat. Nano* **10**, 765 (2015).
- ²⁵ M. Calandra, I. I. Mazin, and F. Mauri, *Phys. Rev. B* **80**, 241108 (2009).
- ²⁶ O. R. Albertini, A. Y. Liu, and M. Calandra, *Phys. Rev. B* **95**, 235121 (2017).
- ²⁷ C. Heil, S. Ponc e, H. Lambert, M. Schlipf, E. R. Margine, and F. Giustino, *Phys. Rev. Lett.* **119**, 087003 (2017).
- ²⁸ L. Hedin, *Phys. Rev.* **139**, A796 (1965).
- ²⁹ M. S. Hybertsen and S. G. Louie, *Phys. Rev. B* **34**, 5390 (1986).
- ³⁰ G. Strinati, H. J. Mattausch, and W. Hanke, *Phys. Rev. Lett.* **45**, 290 (1980).
- ³¹ G. Strinati, H. J. Mattausch, and W. Hanke, *Phys. Rev. B* **25**, 2867 (1982).
- ³² F. Giustino, M. L. Cohen, and S. G. Louie, *Phys. Rev. B* **81**, 115105 (2010).
- ³³ H. Lambert and F. Giustino, *Phys. Rev. B* **88**, 075117 (2013).
- ³⁴ S. Kim and Y.-W. Son, *Phys. Rev. B* **96**, 155439 (2017).
- ³⁵ N. Sirica, S.-K. Mo, F. Bondino, I. Pis, S. Nappini, P. Vilmercati, J. Yi, Z. Gai, P. C. Snijders, P. K. Das, I. Vobornik, N. Ghimire, M. R. Koehler, L. Li, D. Sapkota, D. S. Parker, D. G. Mandrus, and N. Mannella, *Phys. Rev. B* **94**, 075141 (2016).
- ³⁶ S. Ismail-Beigi, *Phys. Rev. B* **73**, 233103 (2006).
- ³⁷ G. Bihlmayer, O. Rader, and R. Winkler, *New J. Phys.* **17**, 050202 (2015).
- ³⁸ G. Dresselhaus, *Phys. Rev.* **100**, 580 (1955).
- ³⁹ O. V. Yazyev, E. Kioupakis, J. E. Moore, and S. G. Louie, *Phys. Rev. B* **85**, 161101 (2012).
- ⁴⁰ P. Hohenberg and W. Kohn, *Phys. Rev.* **136**, B864 (1964).
- ⁴¹ F. Giustino, *Materials Modelling Using Density Functional Theory: Properties and Predictions* (Oxford University Press, Oxford, 2014).
- ⁴² For more extensive and detailed reviews of the development and application of the GW method we refer the reader to Refs. 29, 32, 46, 82–84.
- ⁴³ V. I. Anisimov, *Strong Coulomb Correlations in Electronic Structure Calculations* (CRC Press, 2000).
- ⁴⁴ C. Faber, P. Boulanger, C. Attaccalite, I. Duchemin, and X. Blase, *Phil. Trans. R. Soc. A* **372**, 20130271 (2014).
- ⁴⁵ F. A. Rasmussen and K. S. Thygesen, *J. Phys. Chem. C* **119**, 13169 (2015), <https://doi.org/10.1021/acs.jpcc.5b02950>.
- ⁴⁶ F. Aryasetiawan and O. Gunnarsson, *Rep. Prog. Phys.* **61**, 237 (1998).
- ⁴⁷ S. Baroni, S. de Gironcoli, A. Dal Corso, and P. Giannozzi, *Rev. Mod. Phys.* **73**, 515 (2001).
- ⁴⁸ H.-V. Nguyen, T. A. Pham, D. Rocca, and G. Galli, *Phys. Rev. B* **85**, 081101 (2012).
- ⁴⁹ T. A. Pham, H.-V. Nguyen, D. Rocca, and G. Galli, *Phys. Rev. B* **87**, 155148 (2013).
- ⁵⁰ L. Reining, G. Onida, and R. W. Godby, *Phys. Rev. B* **56**, R4301 (1997).
- ⁵¹ H. F. Wilson, F. Gygi, and G. Galli, *Phys. Rev. B* **78**, 113303 (2008).
- ⁵² P. Umari, G. Stenuit, and S. Baroni, *Phys. Rev. B* **81**, 115104 (2010).
- ⁵³ A more detailed derivation can be found in Ref. 32 and references therein.
- ⁵⁴ S. de Gironcoli, *Phys. Rev. B* **51**, 6773 (1995).
- ⁵⁵ B.-C. Shih, Y. Xue, P. Zhang, M. L. Cohen, and S. G. Louie, *Phys. Rev. Lett.* **105**, 146401 (2010).
- ⁵⁶ M. Schlipf, H. Lambert, N. Zibouche, and F. Giustino, “STERNHEIMERGW,” (2017), doi:10.5281/zenodo.884071.
- ⁵⁷ A. Schindlmayr, P. Garc a-Gonz alez, and R. W. Godby, *Phys. Rev. B* **64**, 235106 (2001).
- ⁵⁸ R. W. Godby and R. J. Needs, *Phys. Rev. Lett.* **62**, 1169 (1989).
- ⁵⁹ H. Vidberg and J. Serene, *J. Low Temp. Phys.* **29**, 179 (1977).
- ⁶⁰ S. Goedecker, M. Teter, and J. Hutter, *Phys. Rev. B* **54**, 1703 (1996).
- ⁶¹ D. M. Ceperley and B. J. Alder, *Phys. Rev. Lett.* **45**, 566 (1980).
- ⁶² J. P. Perdew and A. Zunger, *Phys. Rev. B* **23**, 5048 (1981).
- ⁶³ N. Marzari, A. A. Mostofi, J. R. Yates, I. Souza, and D. Vanderbilt, *Rev. Mod. Phys.* **84**, 1419 (2012).
- ⁶⁴ A. A. Mostofi, J. R. Yates, G. Pizzi, Y.-S. Lee, I. Souza, D. Vanderbilt, and N. Marzari, *Comput. Phys. Commun.* **185**, 2309 (2014).
- ⁶⁵ D. R. Hamann and D. Vanderbilt, *Phys. Rev. B* **79**, 045109 (2009).
- ⁶⁶ G. D. Mahan, *Many-particle Physics* (Springer Science & Business Media, New York, 2013).
- ⁶⁷ C.-H. Park, F. Giustino, M. L. Cohen, and S. G. Louie, *Phys. Rev. Lett.* **99**, 086804 (2007).
- ⁶⁸ A. Kosevich and I. Lifshitz, *Sov. Phys. JETP* **2**, 646 (1956).
- ⁶⁹ W. G. Fisher and M. Sienko, *Inorg. Chem.* **19**, 39 (1980).
- ⁷⁰ H.-P. Komsa and A. V. Krasheninnikov, *Phys. Rev. B* **86**, 241201 (2012).
- ⁷¹ A. Ramasubramaniam, *Phys. Rev. B* **86**, 115409 (2012).
- ⁷² T. Cheiwchanchamnangij and W. R. Lambrecht, *Phys. Rev. B* **85**, 205302 (2012).

- ⁷³ C. Hwang, D. A. Siegel, S.-K. Mo, W. Regan, A. Ismach, Y. Zhang, A. Zettl, and A. Lanzara, *Sci. Rep.* **2**, 590 (2012).
- ⁷⁴ M. L. Trolle, T. G. Pedersen, and V. Véniard, *Sci. Rep.* **7**, 39844 (2017).
- ⁷⁵ M. E. Levinshtein, S. L. Rumyantsev, and M. S. Shur, *Properties of Advanced Semiconductor Materials: GaN, AlN, InN, BN, SiC, SiGe* (John Wiley & Sons, New York, 2001).
- ⁷⁶ X. Xi, Z. Wang, W. Zhao, J.-H. Park, K. T. Law, H. Berger, L. Forró, J. Shan, and K. F. Mak, *Nat. Phys.* **12**, 139 (2016).
- ⁷⁷ J. Wang, F. Ma, and M. Sun, *RSC Adv.* **7**, 16801 (2017).
- ⁷⁸ H. Wang, X. Huang, J. Lin, J. Cui, Y. Chen, C. Zhu, F. Liu, Q. Zeng, J. Zhou, P. Yu, X. Wang, H. He, S. H. Tsang, W. Gao, K. Suenaga, F. Ma, C. Yang, L. Lu, T. Yu, E. H. T. Teo, G. Liu, and Z. Liu, *Nat. Commun.* **8**, 394 (2017).
- ⁷⁹ D. R. Hamann, *Phys. Rev. B* **88**, 085117 (2013).
- ⁸⁰ M. Schlipf and F. Gygi, *Comput. Phys. Commun.* **196**, 36 (2015).
- ⁸¹ S. Grimme, *J. Comput. Chem.* **27**, 1787 (2006).
- ⁸² L. Hedin and S. O. Lundqvist, *Effects of Electron-Electron and Electron-Phonon Interactions on the One-Electron States of Solids*, Vol. 23 (Academic, New York, 1969).
- ⁸³ W. G. Aulbur, M. Städele, and A. Görling, *Phys. Rev. B* **62**, 7121 (2000).
- ⁸⁴ G. Onida, L. Reining, and A. Rubio, *Rev. Mod. Phys.* **74**, 601 (2002).